On the Seasonal variability in the eastern boundary of the North Atlantic Subtropical Gyre

M.D. Pérez-Hernández[1], A. Hernández-Guerra[1], L. Cana-Cascallar[1], C. Arumí-Planas[1], V. Caínzos[1], A. J. González-Santana[2], M. A. Gutierrez-Guerra[2], A. Martínez-Marrero[1], Á. Mosquera Giménez[2], C. Presas Navarro[2], D. Santana-Toscano[1], P. Vélez-Belchí[2]

[1] Unidad Océano y Clima, Instituto de Oceanografía y Cambio Global, IOCAG, Universidad de Las Palmas de Gran Canaria, ULPGC, Unidad Asociada ULPGC-CSIC, Canary Islands, Spain.
[2] Centro Oceanográfico de Canarias, Instituto Español de Oceanografía, Consejo Superior de Investigaciones Científicas, Santa Cruz de Tenerife, Canary Islands, Spain

Key Points:

- The Canary Current varies its path and strength seasonally, moving westward from winter to fall and being the strongest in fall.
- At the Lanzarote Passage the flow is southward throughout the year except in fall when it reverses at surface and intermediate layers.
- The Lanzarote Passage seasonal cycle and its amplitude highly correlates with the seasonal cycle of the Atlantic Meridional Overturning Circulation from the RAPID-MOCHA array.

Keywords: Canary Current, seasonal cycle, Atlantic Meridional Overturning Circulation, Eastern boundary, Lanzarote Passage, North Atlantic Subtropical Gyre.

Abstract

For the first time, four dedicated hydrographic cruises – one in each season – took place in 2015 around the Canary Islands to determinate the seasonality of the flows at the eastern boundary of the North Atlantic Subtropical Gyre. The Canary Current (CC) is the eastern boundary current of the North Atlantic Subtropical Gyre and links the Azores Current with the North Equatorial Current. The CC shows a seasonal behavior in its path and strength, flowing on its easternmost position in winter (3.4±0.3 Sv), through the Canary Islands in spring (2.1±0.7 Sv) and summer (2.0±0.6 Sv) and on its westernmost position in fall (3.2±0.4 Sv). At the Lanzarote Passage (LP), the dominant flow is southward except in fall, where a northward transport is observed at surface (1.1±0.3 Sv) and intermediate (1.3±0.2 Sv) layers. A historical composite observational seasonal cycle is built from all the available estimations on the area and fits the 2015 seasonal cycle. The LP seasonal cycle and seasonal amplitude match the seasonal cycle of the Atlantic Meridional Overturning Circulation (AMOC) measured by the RAPID-MOCHA data array.

1. Introduction

At the eastern region of the North Atlantic Subtropical Gyre, the Canary Current (CC) connects the Azores Current with the North Equatorial Current (Hernández-Guerra et al., 2005; Pérez-Hernández et al., 2013). The first studies carried out in the region used historical hydrographic data to determine the existence of a seasonal change in the structure of the eastern subtropical gyre. These studies found a CC flowing closer to the African coast in summer and through the western islands in winter (Stramma & Isemer, 1988; Stramma & Müller, 1989). Using one hydrographic cruise per season carried out between Madeira and north of the Canary Islands (at 28-32ºN) in 1997 and 1998, Machín et al. (2006) reported that the CC presents a seasonal cycle with a mass transport of 1.7± 1.0 Sv in winter, 2.8± 1.0 Sv in spring, 2.9± 1.1 Sv in summer, and 4.5±1.2 Sv in fall with a shift westward from spring to fall. Pérez-Hernández et al. (2013) confirmed that CC migrates offshore in fall and described a mass transport of 5.8±0.2 Sv southward, west of the Canary Islands. In addition, Fraile-Nuez & Hernández-Guerra (2006) and Mason et al. (2011) found that the variability of the CC is mainly driven by the curl of the wind stress, following the Sverdrup balance.

The area existing between the islands of Lanzarote and Fuerteventura and the African Coast, known as the Lanzarote Passage (LP) has a specific dynamic. Along the LP, Hernández-Guerra et al. (2003), Machín et al. (2006), Pérez-Hernández et al. (2015) and Casanova-Masjoan et al. (2020a) have reported a seasonal variability different than the variability west of the LP. Throughout the year the flow across the LP is southward except during fall, when the flow reverses its direction carrying a mean northward transport of about 2-3 Sv of North Atlantic Central Water (NACW). This northward flow in fall is attributed, using satellite data, to a recirculation of the CC (Pérez-Hernández et al., 2015). In addition, Casanova-Masjoan et al. (2020b) and Hernández-Guerra et al. (2017) have shown, with in situ observations, how a branch of the CC feeds the northward flow at the LP in fall.

The northward flow in surface and thermocline layers along the LP in fall is usually accompanied with a flow at intermediate levels that provides a higher Antarctic Intermediate Water (AAIW) contribution in the area (Fraile-Nuez et al., 2010). This intermediate flow has received the name of intermediate Poleward UnderCurrent (iPUC in Pérez-Hernández et al., 2015), or Canary intermediate Poleward Undercurrent (CiPU in Vélez-Belchí et al., 2021, and used

hereafter), and contributes with nearly 1 Sv to the overall northward transport (Hernández-Guerra et al., 2005, 2017; Laiz et al., 2012; Pérez-Hernández et al., 2015; Vélez-Belchí et al., 2021). For these intermediate layers, Machín et al. (2010) attributed the northward flow during Fall to an isopycnal stretching generated by wind forcing further south. On the other hand, Vélez-Belchí et al. (2021) proposed that the existence of this northward flow at intermediate levels is due to a meridional alongshore pressure gradient generated by the density difference between the Mediterranean Water (MW) and the AAIW.

The Atlantic Meridional Overturning Circulation (AMOC) is an important component of the climate system since it makes the largest oceanic contribution to the meridional transport of heat (Ganachaud, 2003; Caínzos et al., 2022). The strength of the AMOC is continually monitored along 26.5°N by the U.K.–U.S. Rapid Climate Change–Meridional Overturning Circulation and Heatflux Array (hereafter the RAPID-MOCHA array). Chidichimo et al. (2010) found, with the first 4 years of data, a peak-to-peak seasonal cycle of the AMOC of 6.7 Sv, and attributed 5.2 Sv of this seasonal cycle to the eastern boundary. From the three main components of the AMOC at 26.5°N - the Gulf Stream (T_{GS}), Ekman (T_{EK}) and upper-mid-ocean (T_{UMO}) transports - Kanzow et al. (2010) found that T_{UMO} is the largest contributor to the seasonal cycle of the AMOC, with a peak-to-peak seasonal amplitude of 5.9 Sv. Pérez-Hernández et al. (2015) compared the seasonality of the RAPID-MOCHA array to that of the EBC4 mooring located at the Lanzarote Passage (Figure 1) and found significant correlations between the T_{UMO} and both the upper (0.7) and intermediate (0.8) layers of the Lanzarote Passage. This relation is further explored using hydrographic cruises that took place at different years during spring and summer seasons. Vélez-Belchí et al. (2017) and Casanova-Masjoan et al. (2020b) showed a seasonal amplitude of approximately 4 Sv that matches that of the AMOC for the fall-2013/spring-2014 and fall-2016/spring-2017 cruises, while a larger amplitude of nearly 7 Sv was observed for the fall-2017/spring-2018 estimation.

The objective of this paper is to describe the seasonal variability of the circulation in the eastern region of the North Atlantic Subtropical Gyre at the latitude of the Canary Islands by using four identical cruises carried out in each season and, for the first time, in the same year, 2015. The remainder of the paper is organized as follows. In section 2, the different data sets are described. In section 3, we next describe the water masses existing in 2015. Section 4 presents the inverse box model. Section 5 shows the seasonal circulation around the Canary Islands estimated using

the geostrophic approach and the inverse model applied to the hydrographic data. Section 6 discusses the seasonal cycle of 2015 and its amplitude. Section 7 introduces the seasonal cycle of the different AMOC components. Section 8 discusses the results with previous publications to create a composite seasonal cycle from historical data. Section 9 compares the AMOC seasonality with the one described here and finally Section 10 exposes the main conclusions on the manuscript.

2. Data

2.1 Hydrographic data

Since 2003, the *RaProCan* project, the Canary Islands component of the Spanish Institute of Oceanography (IEO) ocean observing system (Tel et al., 2016; Vélez-Belchí et al., 2015), monitors the Canary basin. In 2015, the *RaProCan* project joined efforts with the *Seasonal Variability of the AMOC: Canary Current (SeVaCa*n) project of the Instituto de Oceanografía y Cambio Global (IOCAG-ULPGC) to increase the temporal resolution of the observations. Hence, during 2015, a hydrographic cruise took place in each season (February, April, July and November) to study the seasonal cycle of the basin (Table 1 and Figure 1). These 2015 cruises had a box shaped track around the archipelago consisting of 51 stations divided in 24, 6 and 21 stations for the northern, eastern, and southern transects, respectively (Figure 1). The northern transect of this box samples the 18 standard *RaProCan* stations (from station 6 to 24 in Figure 1, red color). In each station, conductivity, temperature and pressure were measured with redundant temperature and salinity sensors from a Seabird 911+ CTD, which were calibrated at the SeaBird laboratory before the cruise. Onboard salinity calibration was carried out with a Guildline Autosal model 8400B salinometer with a precision better than 0.002 for single samples. At each station, velocity data were acquired from a Lowered Acoustic Doppler Current Profiler (LADCP) system composed of a 150 kHz LADCP downward looking (master) and a 300 kHz LADCP upward looking (slave), with a shared battery pack. The LADCP data were processed according to Fischer and Visbeck (1993). Data were acquired at each station from the surface down to 10 m above the bottom. Distance intervals between stations were approximately 50 km except for the African slope stations, which were 4-5 km apart.

2.2 Surface data.

Maps of Absolute dynamic topography (MADT) were obtained from the Space Oceanographic Division of the Collective Localization Satellites (CLS) through the Archiving,

Validation, and Interpretation of Satellite Oceanographic Data project (AVISO; https://www.aviso.altimetry.fr/en/home.html). The MADT is a merged product from all available Absolute dynamic Topography (ADT) data from TOPEX/Poseidon, Jason-1, Jason-2, Envisat, and GFO satellites. The MSLA data have a temporal resolution of one day and are gridded in 0.25º×0.25º spatial bins on a Mercator grid.

Wind data are estimated using the Weather Research and Forecasting (WRF) model (version 3.9.1), developed at the National Center for Atmospheric Research. This model has the advantage of obtaining wind data in high temporal and spatial resolution in order to resolve the orographic perturbation of the wind as it flows through the islands and the wind variability during the cruise. A complete description of this model can be found in Skamarock et al., (2008). Data from the operational analysis performed every 6 hr, at 1° horizontal resolution at the National Center for Environmental Prediction (NCEP final analysis) were used as initial and boundary conditions for the simulations. For this study, we have set a horizontal grid spacing of 0.125° and 50 terrain-influenced vertical levels. A full description about the configuration of the simulations is given in Cana et al. (2020). Model output, spanning our period of field sampling, includes east-west and north-south wind velocities measured at 10 m (U10 and V10, respectively). Both are used to estimate the Ekman transport to be included in the shallowest layer of the inverse box model.

3. Water Masses

The water masses around the Canary Islands have an interesting seasonal pattern, where not all the water column exhibits changes. Surface waters (SW, γ^n <26.85 kg m^{-3}), as they are in contact with the atmosphere, show the largest seasonal signal being the warmest during fall (reaching up to 25.9ºC) when the trade winds stop, and the coolest during winter (reaching up to 19.0ºC). This is especially remarkable in the open ocean regions (Figure 2 a, b, and c). Immediately beneath this layer, the North Atlantic Central Water (NACW) expands on the density range 26.85 < γ^n < 27.38 kg m^{-3}, following the nearly straight line described in Harvey & Arhan (1988) in all seasons and geographical areas. SW and NACW compose the thermocline layers of our study.

At intermediate levels (27.38< γ^n <27.82 kg m^{-3}), the water mass is a mixture of Antarctic Intermediate Water (AAIW) and Mediterranean Water (MW) (Hernández-Guerra et al., 2005; Machín et al., 2006). Interestingly, the content of AAIW/MW varies seasonally and geographically

in Figure 2. On the northern transect, winter high salinities indicate the presence of a Meddie (Mediterranean Eddy) which is a dynamical structure often seen in the Canary Basin as anticyclonic eddies containing high amount of MW in their core **(**Machín & Pelegrí, 2016) (Figure 2a). In both the northern and southern transects, the intermediate levels barely reveal any seasonality (Figures 2a and c). On the western transect, the intermediate layers transition from a high MW content in summer to the low salinities of AAIW in spring. At the stations sampled along the LP and African shelf (Figure 2 d and e), a clearer transition from MW in winter to AAIW in fall is observed. The presence of AAIW along the African coast in fall has been widely documented (Fraile-Nuez et al., 2010; Hernández-Guerra et al., 2017; Pérez-Hernández et al., 2013; Vélez-Belchí et al., 2017, 2021).

The deepest water mass is North Atlantic Deep Water (NADW, γ^n >27.820 kg m^{-3}), only seen on the open ocean transects (Figure 2a to c). This water mass does not present any seasonality on our dataset.

4. Geostrophic Velocities.

To describe the seasonal change in the ocean circulation in the eastern boundary of the North Atlantic Subtropical Gyre, we have initially estimated the geostrophic velocities using the thermal wind equation with a level of no motion. Here, the density level γ^n=27.975 kg m^{-3} (roughly 1950 m) located at the interface between the MW and the NADW is used for the oceanic waters, while the density level of γ^n=27.380 kg m^{-3} (roughly 750 m) found between the NACW and the AAIW is used for the stations located in the Lanzarote Passage as previous studies carried out in the area (Hernández-Guerra et al., 2005). The geostrophic velocities were integrated along 13 neutral density layers following the water mass characterization given in Section 3 (Table 2). The thermocline waters occupy the first four layers, the intermediate water masses the next two, and the deep-water masses are found in the densest layers corresponding to NADW.

Once the initial geostrophic velocities described above were estimated, an adjustment is carried out in two steps. First, following Comas-Rodríguez et al. (2011) and using the LADCP data, the velocities were adjusted on a station-by-station analysis. This analysis consisted of selecting the vertical range of the LADCP profile where the vertical shear resembles the one of the initial geostrophic velocities, and, then, computing a mean of those vertical LADCP velocities.

Once these reference velocities are added, the new geostrophic transports are computed, but still do not accomplish mass balance for each hydrographic cruise, as shown in Table 3. Second, to reduce the mass transport imbalance obtained using the thermal wind equation and LADCP reference velocities, and therefore increase the reliability of the mass transport estimates, we use an inverse box model. An inverse box model is based on the conservation of mass and allows the estimation of new velocities at the reference level once adjusted to LADCP data. Following Hernández-Guerra et al. (2005) and Pérez-Hernández et al. (2013), we have applied an inverse model to the volume enclosed by the hydrographic stations and the African coast. The box model includes the conservation of mass per layer, the total, and an adjustment for the initial Ekman transport:

$$\iint \quad \rho b \, dx \, dz = -\iint \quad \rho V_{rel} \, dx \, dz + E_k \quad (1)$$

where x and z are the along transect and vertical coordinates, respectively; ρ is the density of each layer. The integral terms are derived from the reference velocity (b) and the relative geostrophic velocity adjusted to LADCP data (V_{rel}). The term E_k designates the Ekman transport. Ekman transport is calculated for each transect and cruise, ranging between –0.32 Sv to 0.36 Sv. The inverse model slightly adjusts these Ekman transports.

Once discretized, the equations of mass transport per layer and the total mass transport form the following matrix equation:

$$A\,x + n = -\Gamma \quad (2)$$

where A is a matrix with the number of layers(Q)×stations(N), n is a column vector whose elements are the noise for each equation, Γ is a vector representing the degree of initial imbalance in each layer, and x is the column vector containing the unknowns of the system:

$$x = \begin{pmatrix} (b_i), i = 1, \dots N_{pair} \\ \Delta T_{Ek} \end{pmatrix} \quad (3)$$

To solve the inverse problem, we apply the Gauss-Markov method which produces a minimum error variance solution from the initial estimates of the unknowns. The solution provided by the method depends on the a priori variances of each component. For mass transport, we have chosen $(0.1 \text{ Sv})^2$ for each layer, and $(1 \text{ Sv})^2$ for the total, and for the velocities $(0.02 \text{ m/s})^2$ for the open ocean stations (>1500 m) and $(0.04 \text{ m/s})^2$ for stations located in shallower waters. For the

winter cruise the a priori variance of the mass transport is slightly different, being $(1\ Sv)^2$ on the first layer, $(0.5\ Sv)^2$ in layers 2 to 7, $(0.25\ Sv)^2$ for the remaining layers, and a $(2\ Sv)^2$ for the total. These a priori variances have been extensively used in the Canary Basin (Hernandez-Guerra et al., 2017; Casanova-Masjoan et al., 2020).

The main outcomes of the inverse modeling are a new set of velocities at the reference level that help to achieve mass balance on the box. As seen in Figure 3 these velocities are mainly non-significantly different from zero. The difference between these velocities and the initial geostrophic velocities referenced to the LADCP measurements is generally small, except on the shallowest areas near the African continent (stations 1-5 and 45-50). The uncertainties are quite similar to the imposed a priori variances, in agreement with other inverse model results.

The velocities at the reference level estimated using the inverse model allow us to compute the adjusted geostrophic mass transport. After the inverse modelling, the initial geostrophic mass transport imbalance estimated with LADCP significantly decreases, being lower than 0.2 Sv for the upper layers (layers 1 to 4), except for summer when it reaches 0.5 Sv, and smaller than 0.1 Sv for the remaining layers as indicated in Table 3. In the following section, the seasonal circulation will be described to estimate the shape of the seasonal cycle for the upper and intermediate layers. The seasonal cycle of the NADW layer will not be studied as the transport is practically not significantly different from zero.

5. Seasonal circulation in 2015.

5.1. The Canary Current and the flow along the African slope.

Figure 4 illustrates the accumulated mass transport of the thermohaline layers and highlights the behavior of the surface layer. Surface transport is also computed for each season from the AVISO MLSA data product. In total, the AVISO estimated transport presents a high correlation with the thermocline transport estimations, ranging from 0.7 to 0.8 for the surface layers (1 and 2), and from 0.6 to 0.8 for the NACW layers (3 and 4) (Table 4). These correlations are higher during the summer cruise and lower during the fall cruise. Though the sign criteria in Figure 4 is negative/positive standing for in/out of the box, hereafter geographical signs will be used (positive being northward/eastward and negative southward/westward). Table 5 shows the transport of each water mass. To allow a better understanding of the flow along the African Slope,

the flow across the northern and southern transects have been split. On the northern transect by the island of Lanzarote and on the southern transect at each side of station 39. The area between Lanzarote and the African shelf is the Lanzarote Passage (Figure 1).

Figure 4 a and Table 5 show that in winter, all the southward flow at the northern transect (-3.4±0.3 Sv) flows east of Lanzarote, through the LP. Likewise, at the southward transect, east of station 40, a mass transport of -2.9±0.4 Sv flows near the African coast (Table 5). Therefore, in winter the CC flows southward across the easternmost stations with a total mass transport of nearly 3 Sv at both the northern and southern transects (Figure 4b). This flow is stronger at the NACW level than at the SW level (Table 5). An inflow of +0.9±0.6 Sv enters the region through the western section and leaves through the southern transect.

In spring, the southward flow concentrates west of Lanzarote (Figure 4 c) and hence, the flow along the African Slope (LP and east of station 39) is very weak (Table 5). Throughout this season, the CC not only shifts westward but also weakens, carrying -2.1±0.7 Sv at the northern transect and -1.2±0.6 Sv at the southern transect (Table 5). The accumulated mass transport and the AVISO geostrophic velocities field suggest that the CC enters in the basin between Lanzarote and station 15 (15.5ºW) and leaves in the vicinity of station 35 (16.9ºW) (Figure 4c and d).

The summer circulation presents a more complex situation where the southward flow of the CC at the northern transect is observed at both sides of Lanzarote (Figure 4e). A steady southward flow of about 1 Sv flows parallel to the African continent crossing the LP and the eastern side of the southern section (Table 5). Figure 4e shows that the second half of the CC flows between Lanzarote and station 15, carrying -2.0±0.6 Sv consistently with Figure 4f. Interestingly, this flow exits the study area through the western transect (Table 5 and Figure 4f). This western diversion of the flow seems to be driven by the large mesoscale features observed in the AVISO field of Figure 4f.

An abrupt change on the circulation is observed in fall when a northward flow appears along the African slope at both the LP (+1.1±0.3 Sv) and the southern transect (+1.7±0.4 Sv) (Figure 4g and Table 5). In addition, a relatively strong flow with a magnitude similar to the CC (+3.2±0.4 Sv) enters the box on the western side (Figure 4g and Table 5). A big portion of it (2.0±0.6 Sv) diverts northward and leaves the box between stations 18 and 20 (Figure 4g and h)

while the remaining part of the flow (-1.4±0.6 Sv) leaves the area through the southern transect around station 32 (Figure 4g and h). In both the AVISO field (Figure 4h) and the accumulated transports (Figure 4g), we can observe the recirculation of the CC taking place as the flow leaves the study area between stations 31-36 and comes back as a northward circulation east of station 36.

In fall, the AVISO field (Figure 4g) shows that the CC flows west of our westernmost stations, and partially enters the area through the western transect. Hence the transport measured on the western transect might underestimate the CC fall transport that has been reported to be as large as 5.8±0.2 Sv (Pérez-Hernández et al., 2013).

5.2. The CiPU and the intermediate circulation.

The intermediate northward flow along the African slope of the CiPU can be observed in three seasons (Table 5). During winter, the CiPU carries a weak transport of +0.3±0.2 Sv across the southern section, and of +0.5±0.1 Sv over the westernmost side of the LP (Table 5 and Figure 5). In summer, while the CiPU at the southern transect is similar to the one in winter (+0.6±0.3 Sv), it decreases considerably at the LP becoming practically negligible (Table 5). In fall, the CiPU reaches its maximum strength carrying northward around 1 Sv in both sections (Table 5 and Figure 5).

During winter, and also in fall a peculiar cyclonic structure appears at the northwestern corner of our study area (Figure 5a, b, and e). During fall, a large structure develops along the southern transect with an identical behavior of the upper layers (Figure 4g and 5a). This structure is the intermediate flow that recirculates together with the upper layers of the CC. In the remaining seasons, a large mesoscale activity exists.

6. The seasonal amplitudes of 2015.

In Figure 6 the seasonal cycle of the CC is defined as in Section 5. For the sake of comparing with previous studies, and due to the presence of large mesoscale features on the southern transect - as a result of the mesoscale structures generated by the islands in the path of the Canary Current and Trade Winds (Borges et al., 2004; Hernández-Guerra et al., 1993) - here we have only considered the transport across the northern section in all seasons for the CC and the

LP. An exception was made for the fall CC since its transport is defined by the flow across the western transect.

The CC has a seasonal cycle that shows a maximum net southward transport in fall and minimum transport in summer (Figure 6a). During fall, both the thermocline and the intermediate layers contribute to the maximum southward transport. However, the transport in fall at the thermocline layer is slightly weaker than the winter estimation. The seasonal amplitude of the CC net transport is 4.5±1.2 Sv, (Table 6). In addition, the intermediate layers have a larger seasonal amplitude (3.3±0.9 Sv) than at thermocline waters (1.4±0.7Sv) (Figure 6a).

Figure 6b reveals that the seasonal amplitude in the LP is dominated by the thermocline layers (see also Table 6 where the). The maximum southward transport at the LP is achieved in winter when the CC flows through it (Figure 4a and b). In contrast, the maximum northward transport occurs in fall, when the CC recirculates northward and the CiPU develops (sections 5.1 and 5.2). The net LP seasonal amplitude of 5.3±0.6 Sv is slightly larger than the seasonal amplitude of the CC.

The seasonal amplitudes for the eastern boundary are next compared with results from previous cruises. Machín et al. (2006) showed a seasonal amplitude for the CC and LP (extending only to the thermocline layers) of 2.2 ±1.0 Sv and 2.8±0.1 Sv, respectively. Their amplitudes are slightly weaker than our thermocline seasonal amplitude estimations (Table 6). Likewise, the comparison with Vélez-Belchí et al. (2017) shows that their estimations of the total seasonal amplitudes (thermocline plus intermediate layers) of the CC (4.1±0.5 Sv) matches our results (4.5±1.2 Sv). In contrast, the amplitude at the LP is weaker (3.7±0.4 Sv) than the 5.3±0.6 Sv estimated in this study. A later study by Casanova-Masjoan et al. (2020) obtains a seasonal amplitude at the LP of 4.2±0.4 Sv to 7.6±0.6 Sv in a few cruises carried out in the period 2016-2018, agreeing with the 5.3±0.6 Sv described here. In both Vélez-Belchí et al. (2017) and Casanova-Masjoan et al. (2020), the seasonal cycle is estimated as the transport difference between a fall and a spring cruise when all the cruises have been carried out in the Canary Islands, which

might not be capturing the full seasonal cycle. For example, in Figure 6 the maximum southward transport at the LP is in winter rather than in spring.

7. A composite seasonal cycle for the CC and LP from previous observations

In Figure 7, all the available observations in the area have been used to compute a composite seasonal cycle for the CC and LP (dots and blue line), and to compare them with the estimations from this work. The longitudinal shifts and thermocline transports of the CC shown in Figure 4 agree with Machín et al. (2006) where the CC is reported to shift westward from spring to fall. However, the winter CC is further east and stronger in our study than in Machín et al. (2006), probably due to the timing of the cruise. The winter cruise took place in their/our study in early-January/mid-February.

In spring and summer, the CC flows through the archipelago mainly along the thermocline layers (Figures 5c and d, 6c and 7a). In spring, the CC matches the estimations of 2.8±0.8 Sv from Machín et al. (2006) and 2.4 ±1.1 Sv from Vélez-Belchí et al. (2017). A stronger flow (3.4 to 3.1 Sv) is reported in Casanova-Masjoan et al. (2020), although their lack of an uncertainty prevents the comparison. Fewer results can be found for summer, where our average southward CC of 2.0±0.6 Sv (Figure 7a) agrees with the 2.9±0.8 Sv reported in Machín et al. (2006) and with the -2.1±0.9 Sv (for 1992) and -2.3±1.1 Sv (for 2011) shown in Hernández-Guerra et al. (2014).

Most of the available measurements of the CC have taken place in fall. Our estimations in this season are 5.6±0.6 Sv southward (3.2±0.4 Sv at surface layers and 2.4±0.5 Sv at intermediate layers, Figures 5e, 6c and 7a). This transport agrees with the 6.5±0.4 Sv described in Vélez-Belchí et al. (2017) for fall 2013. The thermocline transport of the CC in fall is stronger than the 1.5±0.7 Sv estimated in Hernández-Guerra et al., (2017), but lies within the 1.9 to 3.4. Sv range given in Casanova-Masjoan et al. (2020b). In our results the AVISO fields (Figure 4h) suggest that the CC is flowing west of our section and only partially entering our study area. This agrees with previous studies in which stronger transports are reported west of La Palma island (west of 19ºW) as in Hernández-Guerra et al. (2005) (4.7±0.8 Sv) or Pérez-Hernández et al. (2013) (6.2±0.6 Sv).

At the LP, the flow is mainly southward throughout the year except in fall (Figure 7b). In fall, a northward recirculation of the CC through the LP is observed in Figures 4g, h, and 5a, e. This northward recirculation of the CC at surface and intermediate levels is also accompanied with

the onset of the CiPU (Figure 5e). The fall southward to northward reversal transport of the upper layers along the African slope has been widely reported in previous studies with a mass transport ranging between 1 and 3 Sv (Casanova-Masjoan et al., 2020; Fraile-Nuez et al., 2010; Hernández-Guerra et al., 2002, 2017; Knoll et al., 2002; Machín et al., 2006; Pérez-Hernández et al., 2015).

Hence, we can confirm that the seasonal cycle of 2015 matches the historical composite seasonal cycle, and we can add these new estimations to the composite historical seasonal cycle.

8. The seasonal cycle of the eastern boundary and its contribution to the AMOC.

Figure 8 presents the seasonal cycle of the AMOC and each of its components from the RAPID-MOCHA array from 2004 to 2018. The seasonal cycle of the AMOC has an amplitude of about 5.0 Sv (Figure 8a). The Upper-Mid Ocean (T_{UMO}) presents the largest contribution to this seasonal cycle, presenting an amplitude of 5.5 Sv as seen in Figure 8d and described in Chidichimo et al. (2010), Kanzow et al. (2010), and Pérez-Hernández et al. (2015). The AMOC presents three peaks: a minimum in March and two maximums in July-August and in November (Figure 8a). Several studies have described the seasonality of the Ekman transport and the Gulf Stream and have attributed their variability to be the main driver of the July AMOC peak (Atkinson et al., 2010; Meinen et al., 2010). Thus, the uncertainty remains on the effect that the T_{UMO} has on the AMOC, an effect that is related with the winter minimum and the fall maximum that shapes the seasonality of the AMOC. The main contributor to the T_{UMO} seasonal pattern is a positive dynamic height that develops on the eastern basin from August to December (Chidichimo et al., 2010; Kanzow et al., 2010; Pérez-Hernández et al., 2015). Further exploring the structure of the UMO using the dynamic height at the east and west end of the RAPID-MOCHA array, Pérez-Hernández et al. (2015) showed that the UMO seasonal variability is driven by the variability on the eastern boundary.

From the previous section, it is noticeable that the seasonal amplitude of the AMOC (5.0 Sv) and T_{UMO} (5.5 Sv) matches the total seasonal amplitude at the LP (5.3±0.6 Sv). In Pérez-Hernández et al. (2015), a significantly high seasonal correlation (higher than 0.7) was estimated for the T_{UMO} and the transport at the LP at surface and intermediate layers. This was done using data from a mooring located at the LP (the EBC4) and the RAPID-MOCHA array. Here, a similar comparison is done in Figure 9 where the normalized transport of the T_{UMO} is shown together with

a composite historical seasonal cycle estimated for the LP (this cycle is estimated as in Figure 8, including also the 2015 results). The T_{UMO} and the composite LP transport present the same variability and a correlation of 0.8 (p-value 0.003).

9. Conclusions.

In 2015, the *RaProCan* project joined efforts with the *SeVaCan* project to better estimate the seasonal cycle in the eastern boundary of the North Atlantic Subtropical Gyre with cruises carried out during the same year (February, April, July, and November). Seasonal transport estimations for 2015 roughly agree at thermocline layers with the AVISO derived transports. In addition, they also approximately agree with previous estimations carried out in the area with data from either hydrographic cruises or moorings since 2003.

Although both the CC and the LP present similar seasonal amplitudes (4.5±1.2 Sv and 5.3±0.6 Sv, respectively), only the shape of the seasonal cycle at the LP resembles the seasonal cycle of the T_{UMO} (Figure 9). The seasonal cycle at the LP can be summarized as a southward flow that is maximum in winter and that reverses during fall due to the recirculation of the CC and the presence of the northward CiPU. A large agreement has been corroborated between the seasonal cycle amplitude of the LP transport and of the T_{UMO} as previously reported with moorings data in Pérez-Hernández et al (2015), and with hydrographic cruises in Vélez-Belchí et al. (2017), and Casanova-Masjoan et al. (2020). This confirmation has been done with the data from the four hydrographic cruises used in this study, and also with the total historical hydrographic data compiled in the area. Hence this study concludes that the LP and T_{UMO} have similar seasonal transport amplitudes (ca. 5 Sv), and that their seasonal cycle has a 0.8 correlation coefficient. On early studies, part of this seasonality was explained with a Rossby wave model (Kanzow et al., 2010; Pérez-Hernández et al., 2015), although Vélez-Belchí et al. (2017) showed that this model was very dependent on the longitudinal extend of the wind-stress chosen.

Acknowledgments

This study has been performed as part of the Instituto Español de Oceanografía *RaProCan* project, and as a part of the *SeVaCan* project (CTM2013–48695) from the Ministerio de Economía y Competividad. This article is a publication of the Unidad Océano y Clima from Universidad de

Las Palmas de Gran Canaria, an R&D&I CSIC-associate unit. The wind data were collected from NCEP Reanalysis Derived data (http://www.eslr.noaa.gov/psd/). V.C., C.A.-P. acknowledge the Agencia Canaria de Investigación, Innovación y Sociedad de la Información (ACIISI) grant program of "Apoyo al personal investigador en formación". D. S.-T. acknowledges the "Ministerio de Universidades" grant program of "Formación de Profesorado Universitario" for the grant FPU20/02211. The authors are grateful to the captain and crew of the R/V Ángeles Alvariño for their help at sea.

References

Atkinson, C., Bryden, H. L., Hirschi, J. J.-M., & Kanzow, T. (2010). On the seasonal cycles and variability of Florida Straits, Ekman and Sverdrup transports at 26° N in the Atlantic Ocean. *Ocean Science*, *6*, 837–859. https://doi.org/https://doi.org/10.5194/os-6-837-201

Borges, R., & Hernández-Guerra, A. (2004) Analysis of sea surface temperature time series of the south-eastern North Atlantic, International Journal of Remote Sensing, 25:5, 869-891, DOI: 10.1080/0143116031000082442

Cana, L., Grisolía-Santos, D., & Hernández-Guerra, A. (2020). A Numerical Study of a Sea Breeze at Fuerteventura Island, Canary Islands, Spain. *Boundary-Layer Meteorology*, *175*(2), 277–296. https://doi.org/10.1007/s10546-020-00506-z

Caínzos, V., Hernández-Guerra, A., McCarthy, G.D., McDonagh, E.L., Cubas Armas, M., & Pérez Hernández, M.D. (2022). Thirty years of GOSHIP and WOCE data: Atlantic Overturning of mass, heat and freshwater transport. *Geophysical Research Letters*, 49 e2021GL096527. https://doi.org/10.1029/2021GL096527

Casanova-Masjoan, M., Pérez-Hernández, M. D., Vélez-Belchí, P., Cana, L., & Hernández-Guerra, A. (2020). Variability of the Canary Current Diagnosed by Inverse Box Models. *Journal of Geophysical Research: Oceans*, *125*(8). https://doi.org/10.1029/2020JC016199

Chidichimo, M. P., Kanzow, T., Cunningham, S. A., Johns, W. E., & Marotzke, J. (2010). The contribution of eastern-boundary density variations to the Atlantic meridional overturning circulation at 26.5° N. *Ocean Science*, *6*(2), 475–490. https://doi.org/10.5194/os-6-475-2010

Comas-Rodríguez, I., Hernández-Guerra, A., Fraile-Nuez, E., Martínez-Marrero, A., Benítez-Barrios, V. M., Pérez-Hernández, M. D., & Vélez-Belchí, P. (2011). The Azores Current System from a meridional section at 24.5°W. *Journal of Geophysical Research: Oceans*, *116*(9). https://doi.org/10.1029/2011JC007129

Fischer, J., & Visbeck, M. (1993). Seasonal variation of the daily zooplankton migration in the Greenland sea. *Deep Sea Research Part I: Oceanographic Research Papers*, *40*(8), 1547–1557. https://doi.org/10.1016/0967-0637(93)90015-U

Fraile-Nuez, E., & Hernández-Guerra, A. (2006). Wind-driven circulation for the eastern North Atlantic Subtropical Gyre from Argo data. *Geophysical Research Letters*, *33*(3), 1–4. https://doi.org/10.1029/2005GL025122

Fraile-Nuez, E., MacHín, F., Vélez-Belchí, P., López-Laatzen, F., Borges, R., Benítez-Barrios, V., & Hernández-Guerra, A. (2010). Nine years of mass transport data in the eastern boundary of the

North Atlantic Subtropical Gyre. *Journal of Geophysical Research: Oceans*, *115*(9). https://doi.org/10.1029/2010JC006161

Ganachaud, A. (2003). Large-scale mass transports, water mass formation, and diffusivities estimated from World Ocean Circulation Experiment (WOCE) hydrographic data. *Journal of Geophysical Research*, *108*(C7), 3213. https://doi.org/10.1029/2002JC001565

Harvey, J., & Arhan, M. (1988). The Water Masses of the Central North Atlantic in 1983—84. *Journal of Physical Oceanography*. https://doi.org/10.1175/1520-0485(1988)018<1855:twmotc>2.0.co;2

Hernández-Guerra, A., Aristegui, A., Cantón, M., & Nykjaer, L., (1993). Phytoplankton pigment patterns in the Canary Islands área as determined using Coastel Zone Colour Scanner data. *International Journal of Remote Sensing*. 14:7, 1431-1437. 10.1080/01431169308953977.

Hernández-Guerra, A., Machín, F., Antoranz, A., Cisneros-Aguirre, J., Gordo, C., Marrero-Díaz, A., et al. (2002). Temporal variability of mass transport in the Canary Current. *Deep-Sea Research Part II: Topical Studies in Oceanography*, *49*(17), 3415–3426. https://doi.org/10.1016/S0967-0645(02)00092-9

Hernández-Guerra, A., Pelegrí, J. L., Fraile-Nuez, E., Benítez-Barrios, V., Emelianov, M., Pérez-Hernández, M. D., & Vélez-Belchí, P. (2014). Meridional overturning transports at 7.5N and 24.5N in the Atlantic Ocean during 1992-93 and 2010-11. *Progress in Oceanography*, *128*. https://doi.org/10.1016/j.pocean.2014.08.016

Hernández-Guerra, Alonso, Fraile-Nuez, E., Borges, R., López-Laatzen, F., Vélez-Belchí, P., Parrilla, G., & Müller, T. J. (2003). Transport variability in the Lanzarote passage (eastern boundary current of the North Atlantic subtropical Gyre). *Deep-Sea Research Part I: Oceanographic Research Papers*, *50*(2), 189–200. https://doi.org/10.1016/S0967-0637(02)00163-2

Hernández-Guerra, Alonso, Fraile-Nuez, E., López-Laatzen, F., Martínez, A., Parrilla, G., & Vélez-Belchí, P. (2005). Canary Current and North Equatorial Current from an inverse box model. *Journal of Geophysical Research: Oceans*, *110*(12), 1–16. https://doi.org/10.1029/2005JC003032

Hernández-Guerra, Alonso, Espino-Falcón, E., Vélez-Belchí, P., Dolores Pérez-Hernández, M., Martínez-Marrero, A., & Cana, L. (2017). Recirculation of the Canary Current in fall 2014. *Journal of Marine Systems*, *174*, 25–39. https://doi.org/10.1016/j.jmarsys.2017.04.002

Kanzow, T., Cunningham, S. A., Johns, W. E., Hirschi, J. J.-M., Marotzke, J., Baringer, M. O., et al. (2010). Seasonal Variability of the Atlantic Meridional Overturning Circulation at 26.5°N. *Journal of Climate*, *23*(21), 5678–5698. https://doi.org/10.1175/2010JCLI3389.1

Knoll, M., Hernández-Guerra, A., Lenz, B., López Laatzen, F., Machín, F., Müller, T. J., & Siedler, G. (2002). The Eastern Boundary Current system between the Canary Islands and the African Coast. *Deep-Sea Research Part II: Topical Studies in Oceanography*, *49*(17), 3427–3440. https://doi.org/10.1016/S0967-0645(02)00105-4

Laiz I., Pelegrí J.L., Machín, F., Sangrà P., Hernández-Guerra, A., Marrero-Díaz, A., & Rodríguez-Santana, A. (2012). Easter boundary drainage of the North Atlantic subtropical gyre. O*cean Dynamics*, 62:1287-1310. 10.1007/s10236-012-0560-6

Machín, F., Hernández-Guerra, A., & Pelegrí, J. L. (2006). Mass fluxes in the Canary Basin. *Progress in Oceanography*, *70*(2–4), 416–447. https://doi.org/10.1016/j.pocean.2006.03.019

Machín, F.., & Pelegrí, J. L. (2016). Interaction of Mediterranean Water lenses with Antarctic Intermediate Water off Northwest Africa. *Scientia Marina*, *80*(S1), 205–214. https://doi.org/10.3989/scimar.04289.06A

Machín, F., Pelegrí, J. L., Fraile-Nuez, E., Vélez-Belchí, P., López-Laatzen, F., & Hernández-Guerra, A. (2010). Seasonal flow reversals of intermediate waters in the canary current system east of the canary Islands. *Journal of Physical Oceanography*, *40*(8), 1902–1909. https://doi.org/10.1175/2010JPO4320.1

Mason, E., Colas, F., Molemaker, J., Shchepetkin, A. F., Troupin, C., McWilliams, J. C., & Sangrà, P. (2011). Seasonal variability of the Canary Current: A numerical study. *Journal of Geophysical Research: Oceans*, *116*(6), 1–20. https://doi.org/10.1029/2010JC006665

Meinen, C. S., Baringer, M. O., & Garcia, R. F. (2010). Florida Current transport variability: An analysis of annual and longer-period signals. *Deep Sea Research Part I: Oceanographic Research Papers*, *57*(7), 835–846. https://doi.org/10.1016/j.dsr.2010.04.001

Pérez-Hernández, M. D., Hernández-Guerra, A., Fraile-Nuez, E., Comas-Rodríguez, I., Benítez-Barrios, V. M., Domínguez-Yanes, J. F., et al. (2013). The source of the Canary current in fall 2009. *Journal of Geophysical Research: Oceans*, *118*(6). https://doi.org/10.1002/jgrc.20227

Pérez-Hernández, M. D., McCarthy, G. D., Vélez-Belchí, P., Smeed, D. A., Fraile-Nuez, E., & Hernández-Guerra, A. (2015). The Canary Basin contribution to the seasonal cycle of the Atlantic Meridional Overturning Circulation at 26°N. *Journal of Geophysical Research: Oceans*, *120*(11). https://doi.org/10.1002/2015JC010969

Skamarock, W. C., Klemp, J. B., Dudhia, J., & Gill, D. O. (2008). *A Description of the Advanced Research WRF Version 3*. https://doi.org/10.13140/RG.2.1.2310.6645

Stramma, L., & Isemer, H. (1988). Seasonal variability of meridional temperature fluxes. *Journal of Marine Research*, *46*(2), 281-299.

Stramma, L., & Müller, T. J. (1989). Some observations of the Azores Current and the North Equatorial Current. *Journal of Geophysical Research*, *94*(C3), 3181. https://doi.org/10.1029/jc094ic03p03181

Tel, E., Balbin, R., Cabanas, J.-M., Garcia, M.-J., Garcia-Martinez, M. C., Gonzalez-Pola, C., et al. (2016). IEOOS: the Spanish Institute of Oceanography Observing System. *Ocean Science*, *12*(2), 345–353. https://doi.org/10.5194/os-12-345-2016

Vélez-Belchí, P., González-Carballo, M., Pérez-Hernández, M. D., & Hernández-Guerra, A. (2015). Oceanographic and biological features in the Canary Current Large Marine Ecosystem. In *115* (pp. 299–308). Paris: IOC-UNESCO.

Vélez-Belchí, P., Pérez-Hernández, M. D., Casanova-Masjoan, M., Cana, L., & Hernández-Guerra, A. (2017). On the seasonal variability of the Canary Current and the Atlantic Meridional Overturning Circulation. *Journal of Geophysical Research: Oceans*, *122*(6). https://doi.org/10.1002/2017JC012774

Vélez-Belchí, Pedro, Caínzos, V., Romero, E., Pérez-Hernández, M. D., & Hernández-Guerra, A. (2021). The Canary intermediate poleward undercurrent: not another poleward undercurrent in an eastern boundary upwelling system. *Journal of Physical Oceanography*, *in press*.

Tables

Table 1. Hydrographic cruises

Cruise	Dates	Number of stations
SeVaCan1502	26 February / 6 March 2015	51
RaProCan1504	07-15 April 2015	51
SeVaCan1507	17-25 July 2015	51
RaProCan1510	01-09 October 2015	51

Table 2. Deepest limit (dbar) of the γ^n isoneutral layers used in the mass transport analyses

Layer	**γ^n (kg m^{-3})**	**Deepest limit (dbar)**	**Water masses**
1	26.440	20	SW
2	26.850	298	SW
3	27.162	540	NACW
4	27.380	740	NACW
5	27.620	967	AAIW
6	27.820	1314	AAIW MW
7	27.922	1656	NADW
8	27.975	2015	NADW
9	28.008	2241	NADW
10	28.044	2592	NADW
11	28.072	2965	NADW
12	28.0986	3519	NADW
13	28.1295 (Bottom)	3923	NADW

Table 3. Accumulated imbalance (in Sv) for the net transport of each water mass after applying the LADCP correction to each cruise and after the inverse box model.

Cruise	Imbalance after LADCP			Imbalance after inverse box modelling		
	SW/NACW	AAIW/MW	NADW	SW/NACW	AAIW/MW	NADW
SeVaCan1502	0.78	0.12	1.41	0.2±0.1	-0.1±0.1	-0.1±0.2
RaProCan1504	0.20	-0.13	0.78	0.1±0.1	0.0±0.1	0.0±0.2
SeVaCan1507	2.08	0.00	-1.33	0.5±0.2	-0.1±0.1	-0.0±0.2
RaProCan1510	-4.49	-3.25	-8.51	0.2±0.1	0.0±0.1	0.1±0.2

Table 4. Correlations between the accumulated mass transport at surface (layers 1 to 2 from Table 2) and NACW (layers 3 to 4 from Table 2) layers and the estimated accumulated mass transport from AVISO per season. In between brackets the p-value is shown, and non-significant correlations have been marked with an *.

	Winter		**Spring**		**Summer**		**Fall**	
	SW	**NACW**	**SW**	**NACW**	**SW**	**NACW**	**SW**	**NACW**
Lanzarote Passage	0.91 (0.00)	0.95 (0.00)	-0.32 (0.37)*	0.59 (0.00)	0.82 (0.00)	0.74 (0.00)	0.80 (0.01)	0.44 (0.00)
Northern transect	0.00 (0.98)*	-0.40 (0.15)*	0.63 (0.01)	0.38 (0.29)*	0.80 (0.00)	-0.66 (0.04)	0.41 (0.13)*	0.45 (0.19)*
West transect	0.94 (0.00)	0.96 (0.00)	0.65 (0.11)*	0.52 (0.04)	0.55 (0.20)*	0.58 (0.02)	0.57 (0.20)*	0.19 (0.49)*
Southern transect	0.59 (0.00)	0.61 (0.00)	0.91 (0.00)	0.65 (0.11)	0.93 (0.00)	0.48 (0.28)	0.84 (0.00)	0.71 (0.08)*
total	0.76 (0.00)	0.69 (0.00)	0.85 (0.00)	0.61 (0.00)	0.84 (0.00)	0.83 (0.00)	0.75 (0.00)	0.65 (0.00)

Table 5. Estimated seasonal transports (Sv) for the different transects. For the northern and southern transects the flow is split between that East (African Slope - Afr. Slp.) and West of Lanzarote (W. of Lz.), and East/West of station 40 for SW and NACW and of station 42 for the intermediate waters (IW), respectively. SW is for the surface waters (layers 1 and 2 in Table 2), NACW for the North Atlantic Central Water layer (layers 3 and 4 in Table 2), and IW is for the intermediate water layer (layers 5 and 6 in Table 2). The sign convection of this table is geographical (positive to the north/east and negative to the south/west).

		Winter		**Spring**		**Summer**		**Fall**	
		North	**South**	**North**	**South**	**North**	**South**	**North**	**South**
Afr. Slp.	**SW**	-1.3±0.2	-1.3±0.3	-0.3±0.1	-1.1±0.2	-1.0±0.1	-1.2±0.1	-0.2±0.1	-0.3±0.2
	NACW	-2.1±0.3	-1.6±0.3	0.3±0.2	0.3±0.3	-0.1±0.3	0.2±0.3	1.3±0.3	1.9±0.3
	Total	-3.4±0.3	-2.9±0.4	0.0±0.3	-0.7±0.3	-1.1±0.3	-1.0±0.4	1.1±0.3	1.7±0.4
	IW	0.5±0.1	0.3±0.2	0.0±0.2	-0.1±0.3	0.2±0.2	0.6±0.3	1.3±0.2	1.1±0.3
W. of Lz.	**SW**	-0.4±0.6	-0.6±0.6	-1.1±0.5	-1.0±0.4	-1.2±0.2	-0.2±0.3	0.4±0.3	-0.3±0.2
	NACW	0.6±0.5	-0.7±0.5	-1.0±0.7	-0.1±0.4	-0.8±0.5	-0.2±0.4	1.6±0.5	-1.1±0.5
	Total	0.2±0.8	-1.3±0.8	-2.1±0.7	-1.2±0.6	-2.0±0.6	-0.4±0.5	2.0±0.6	-1.4±0.6
	IW	2.1±0.8	0.9±0.8	0.1±0.8	3.3±0.7	0.9±0.6	-0.2±0.6	2.5±0.7	0.2±0.7
Western	**SW**	-0.1±0.4		0.5±0.3		-1.2±0.2		1.1±0.2	
	NACW	1.0±0.4		-0.8±0.4		-0.9±0.4		2.1±0.3	
	Total	0.9±0.6		-0.3±0.5		-2.1±0.4		3.2±0.4	
	IW	1.5±0.6		-1.6±0.5		0.8±0.5		2.4±0.5	

Table 6. Transport seasonal amplitudes (Sv) for the LP, for the CC and for the eastern boundary, computed for the net transport, as well as for its division into thermocline and intermediate layers.

	LP	**CC**	**East. boundary**
Thermocline	4.5±0.4	1.4±0.7	6.5±0.2
Intermediate	1.3±0.4	3.3±0.9	3.8±0.4
Net	5.3±0.6	4.5±1.2	9.1±0.4

Figure 1. Map of the study area showing the main topographic and geographical features referred to in the text. The black circles are the stations sampled in each 2015 cruise, while the standard *RaProCan* stations are highlighted in red. One in every five stations for each cruise has been labeled. The asterisks indicate the position of the main moorings of the RAPID-MOCHA array at the eastern boundary and the mooring EBC4.

Figure 2. Seasonal θ/S diagram for each relevant geographical location: (a) Northern transect (stations 11 to 24), (b) Western transect (stations 25 to 30), (c) Southern transect (stations 31 to 46), (d) Lanzarote Passage (stations 1 to 10), and (e) Cape Juby (stations 47 to 51). Each hydrographic cruise is represented in a different color, being blue for winter, green for spring, red for summer and orange for fall. The grey thick lines correspond to the isoneutrals used in the inverse model to divide the water column into surface, central, intermediate and deep (Table 2). NACW stands for North Atlantic Central Water, MW for Mediterranean Waters, AAIW for Antarctic Intermediate Waters, and NADW for North Atlantic Deep Waters.

Figure 3. Velocities at the reference level for each station pair determined by the ADCP (red) and by the ADCP plus the inverse calculations with their error bars (black) for each season/cruise. (a) Winter - SeVaCan1502, (b) Spring - RaProCan1504, (a) Summer - SeVaCan1507 and (d) Fall - RaProCan1510.

Figure 4. On the left panel: Accumulated mass transport in the thermocline layers during the (a) winter, (c) spring, (e) summer, and (g) fall cruises for the surface (layers 1:2 in blue), and the thermocline layers (layers 1:4 in black). The accumulated mass transport obtained using the surface geostrophic velocities from the AVISO MSLA product integrated to the depth corresponding to the lower limit of the seasonal thermocline waters (27.38 kg m^{-3}) are also shown (dashed blue). For reference, the bathymetry has been superimposed, a vertical black line indicates the corner of each track labelled in the lower panel. The sign convection of this figure is negative/positive standing for in/out of the box. On the right panel: AVISO Absolute Dynamic Topography (ADT) and geostrophic velocities for the (b) winter, (d) spring, (f) summer, and (h) fall cruises together with a schematic representation of the main transports.

Figure 5. (a) Accumulated mass transport for the intermediate layers during (blue) winter, (green) spring, (red) summer, and (orange) fall cruises. For reference, the bathymetry has been superimposed,

a vertical black line indicates the corner of each track labelled in the lower panel. The sign convection of this figure is negative/positive standing for in/out of the box. The right panels are identical to the one of Figure 4 but adding the schematic representation of the main intermediate circulation features with green arrows and labels for (b) winter, (c) spring, (d) summer and (e) fall.

Figure 6. Seasonal cycle of the estimated transports on the thermocline layer (blue line), intermediate layer (green line) and the net (black line) for (a) CC and (b) the Lanzarote Passage.

Figure 7. Total seasonal cycle (red line) for 2015 together with all the historical measurements (color dots) for the Canary Current (a) and Lanzarote Passage (b). An average composite seasonal cycle done with all the historical measurements is shown with its standard deviation (blue line and error bars).

Figure 8. Seasonal cycles of the transport (Sv) of the AMOC (a) and its main components: the Gulf Stream (b), Ekman Transport (c) and Upper-Mid Ocean (d) computed using the RAPID-MOCHA time series. Note different y-axis ranges in each plot

Figure 9. Seasonal cycles of standardized transports (Sv) of the Upper-Mid Ocean (red) obtained from the RAPID-MOCHA array and of the historical composite seasonal cycle at the Lanzarote Passage (blue).

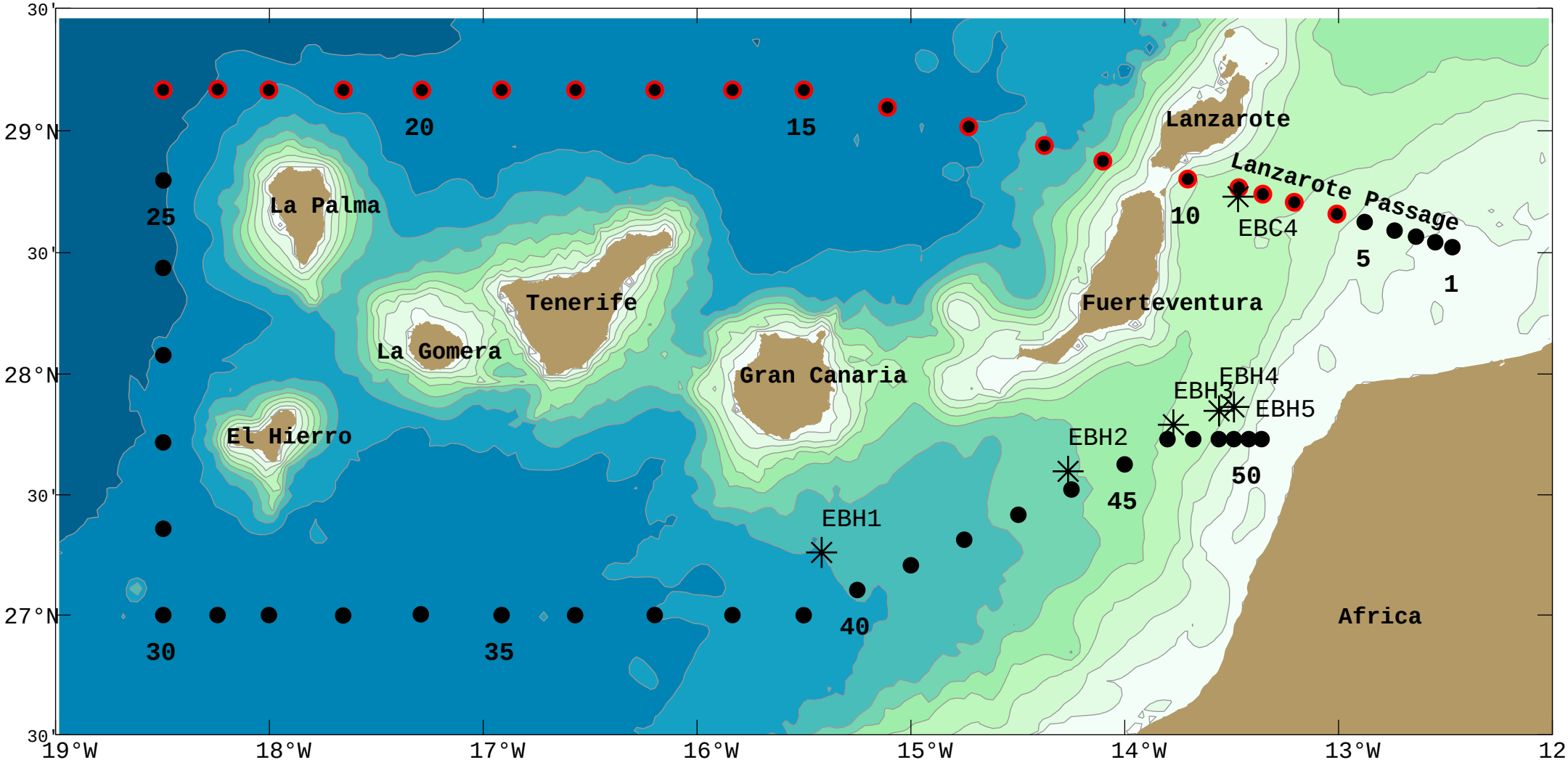
30'
29°N
30'
28°N
30'
27°N
30'
19°W
18°W
17°W
16°W
15°W
14°W
13°W
12°W
La Palma
El Hierro
La Gomera
Tenerife
Gran Canaria
Fuerteventura
Lanzarote
Lanzarote Passage
Africa
EBC4
EBH1
EBH2
EBH3
EBH4
EBH5
20
15
25
10
5
1
50
45
40
30
35

Figure 1

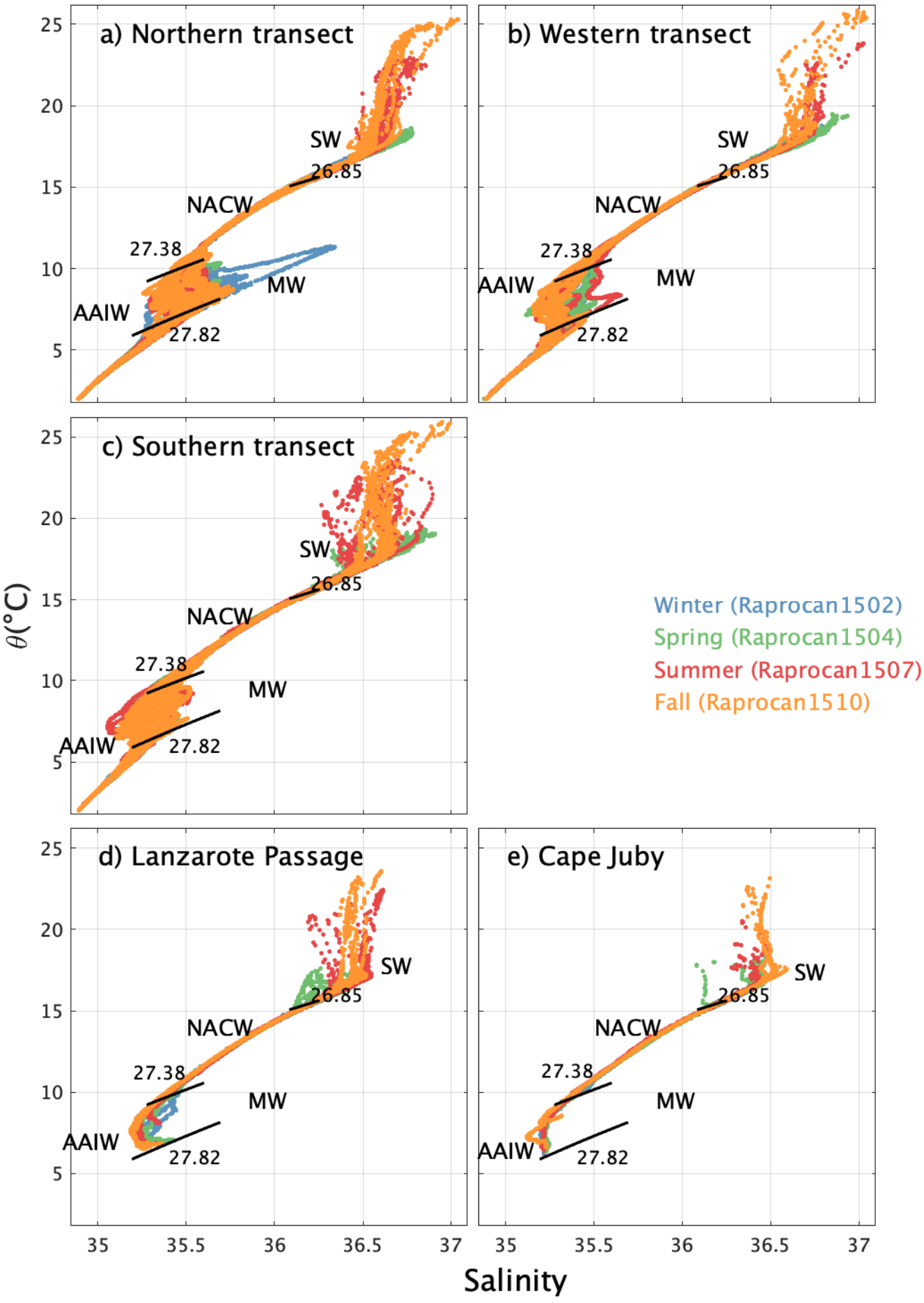
a) Northern transect
b) Western transect
c) Southern transect
d) Lanzarote Passage
e) Cape Juby
SW
26.85
NACW
27.38
MW
AAIW
27.82
θ(°C)
Salinity
Winter (Raprocan1502)
Spring (Raprocan1504)
Summer (Raprocan1507)
Fall (Raprocan1510)

Figure 2

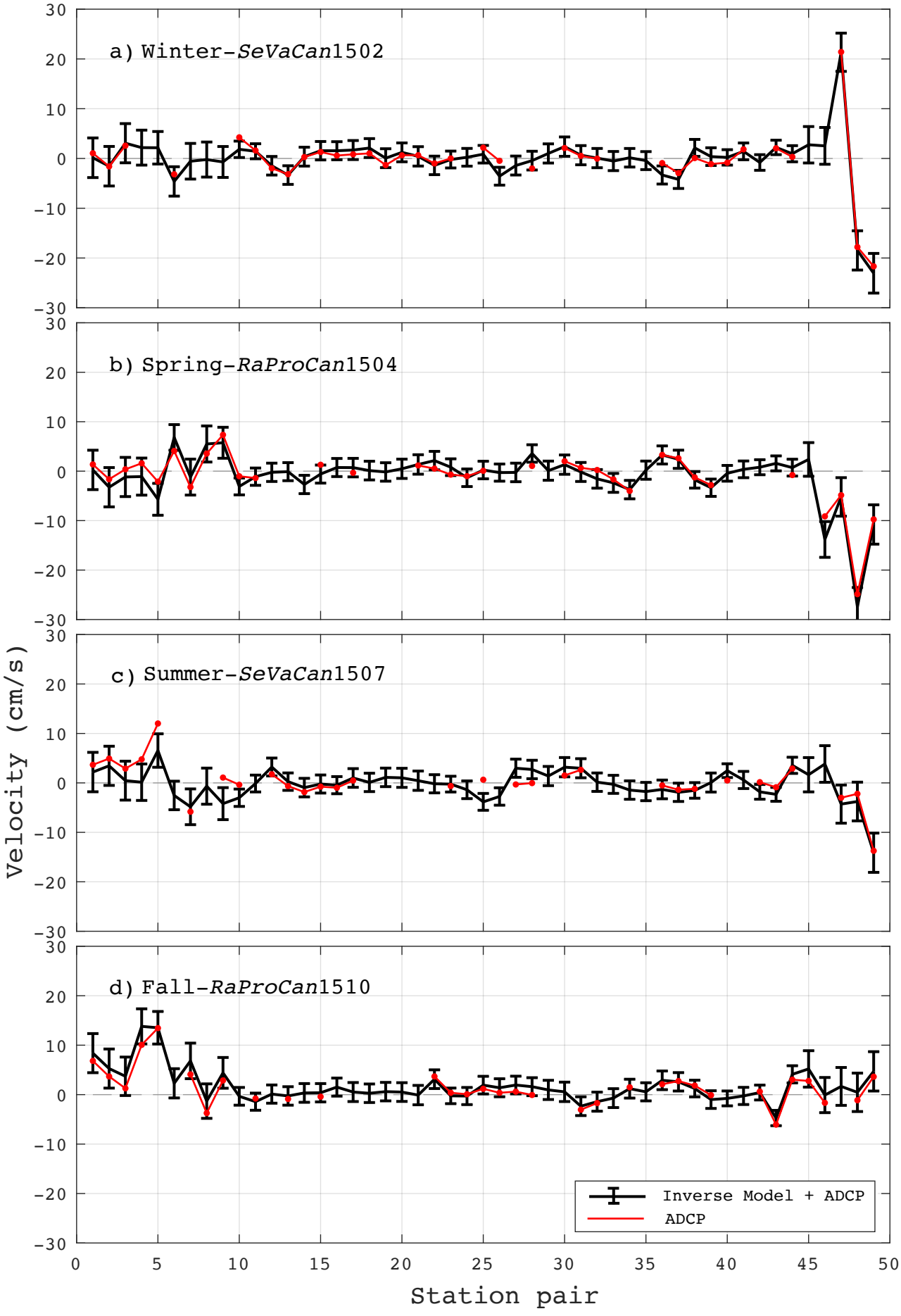
a) Winter-SeVaCan1502
b) Spring-RaProCan1504
c) Summer-SeVaCan1507
d) Fall-RaProCan1510
Velocity (cm/s)
Station pair
Inverse Model + ADCP
ADCP

Figure 3

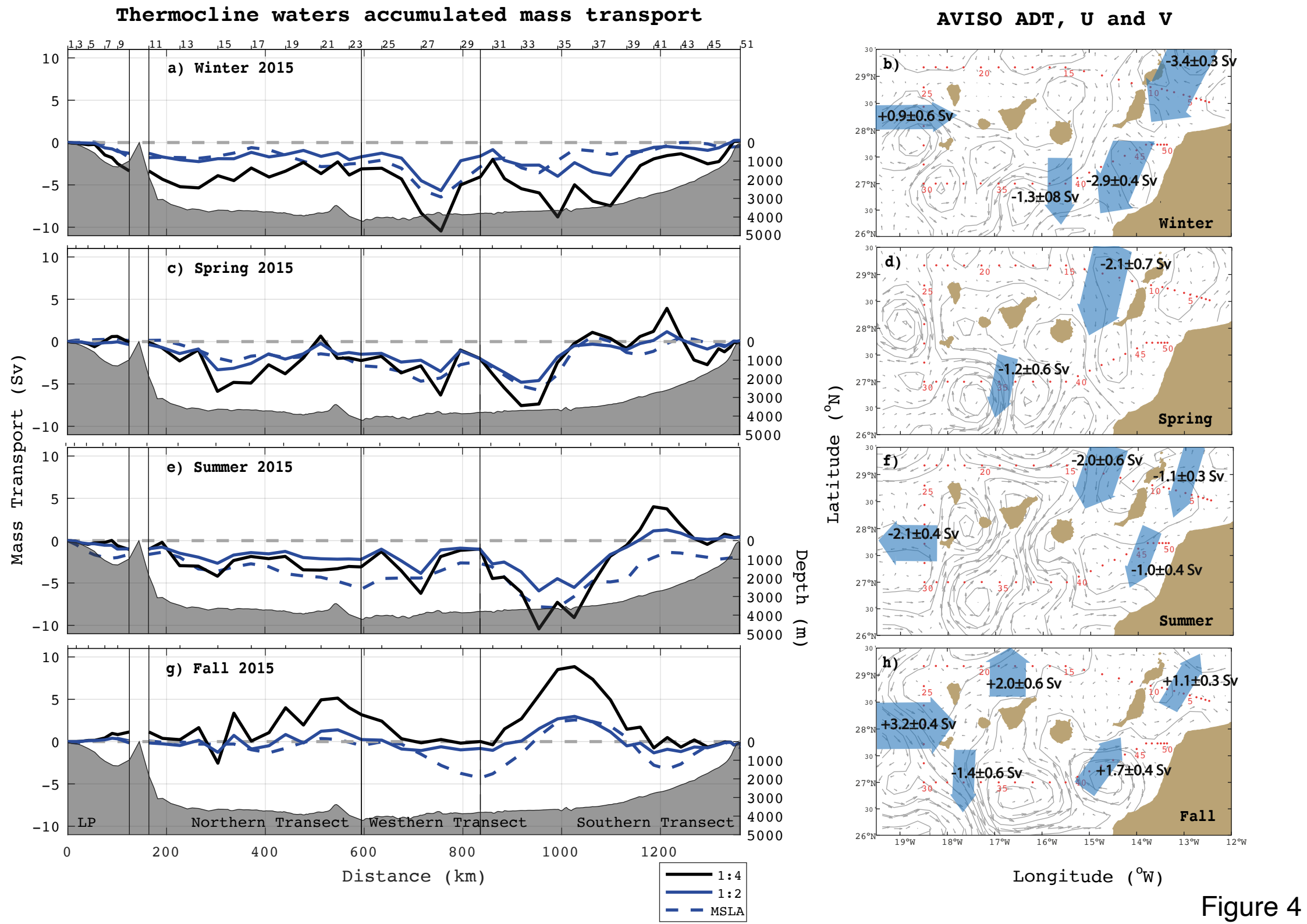
Thermocline waters accumulated mass transport
a) Winter 2015
c) Spring 2015
e) Summer 2015
g) Fall 2015
LP
Northern Transect
Westhern Transect
Southern Transect
Mass Transport (Sv)
Depth (m)
Distance (km)
1:4
1:2
MSLA
AVISO ADT, U and V
b)
-3.4±0.3 Sv
+0.9±0.6 Sv
-2.9±0.4 Sv
-1.3±08 Sv
Winter
d)
-2.1±0.7 Sv
-1.2±0.6 Sv
Spring
f)
-2.0±0.6 Sv
-1.1±0.3 Sv
-2.1±0.4 Sv
-1.0±0.4 Sv
Summer
h)
+2.0±0.6 Sv
+1.1±0.3 Sv
+3.2±0.4 Sv
-1.4±0.6 Sv
+1.7±0.4 Sv
Fall
Latitude (°N)
Longitude (°W)

Figure 4

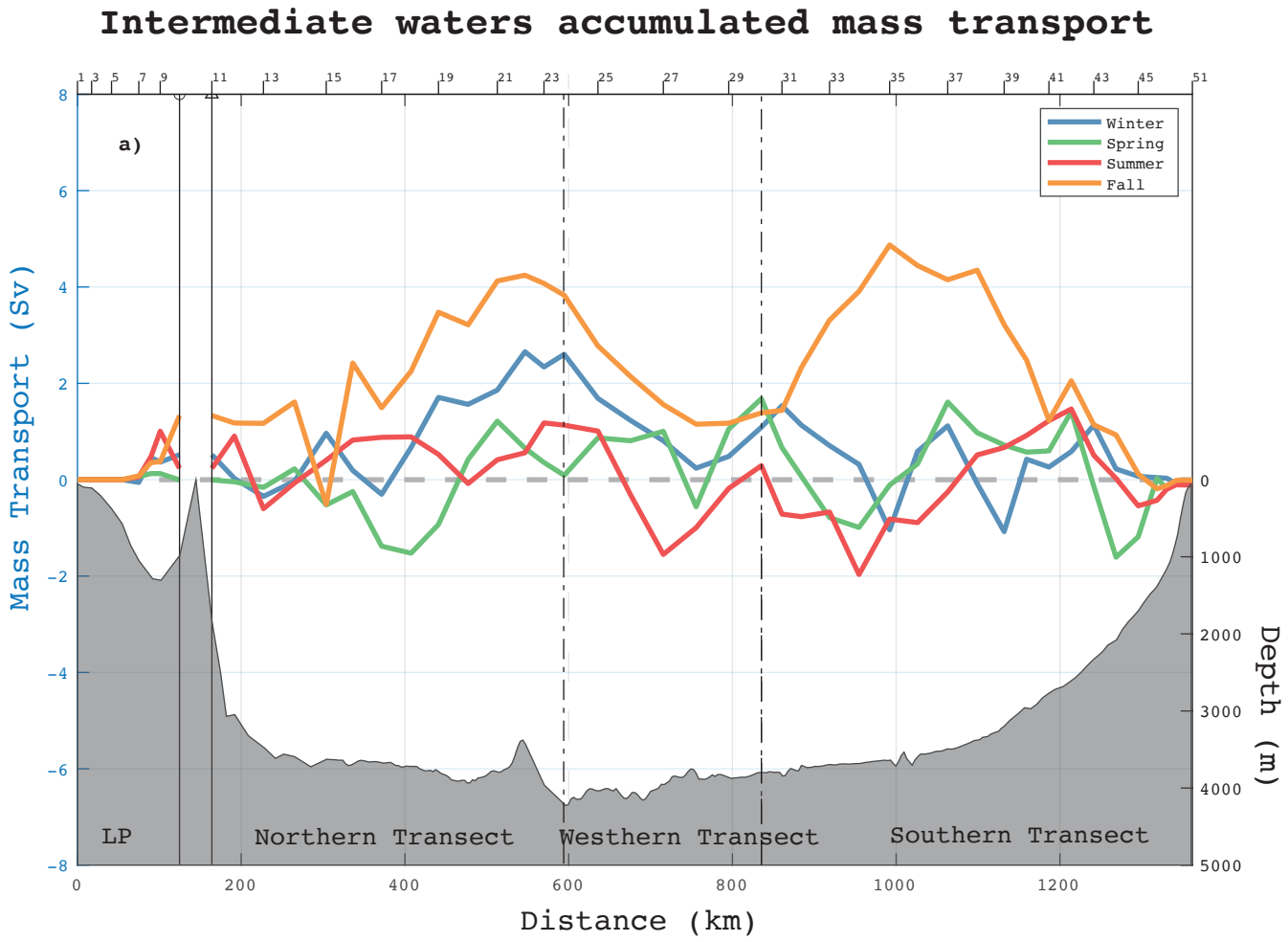
Intermediate waters accumulated mass transport
a)
Winter
Spring
Summer
Fall
Mass Transport (Sv)
Depth (m)
Distance (km)
LP
Northern Transect
Westhern Transect
Southern Transect

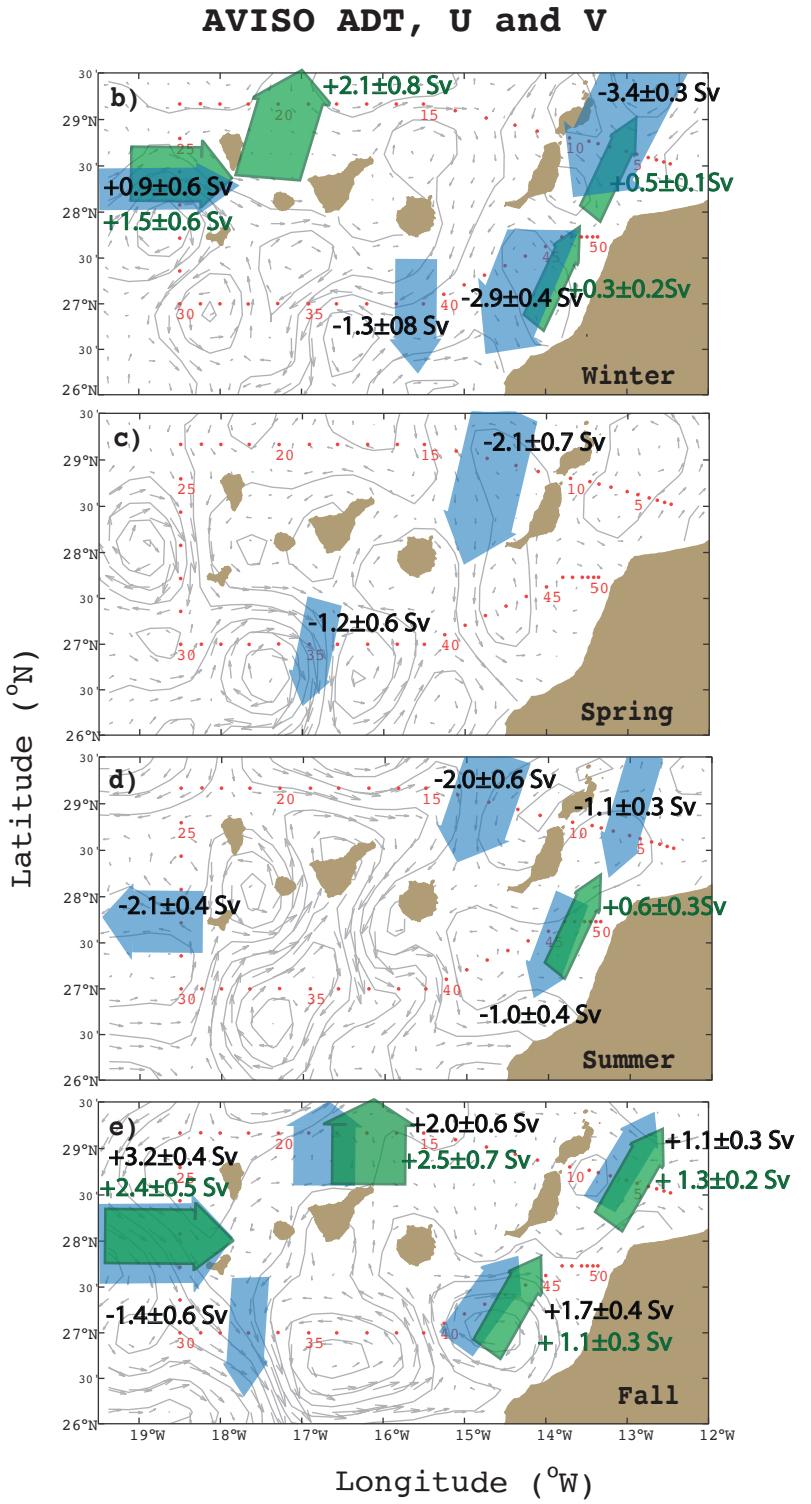
AVISO ADT, U and V
b)
+2.1±0.8 Sv
-3.4±0.3 Sv
+0.9±0.6 Sv
+1.5±0.6 Sv
-0.5±0.1Sv
-2.9±0.4 Sv
+0.3±0.2Sv
-1.3±08 Sv
Winter
c)
-2.1±0.7 Sv
-1.2±0.6 Sv
Spring
d)
-2.0±0.6 Sv
-1.1±0.3 Sv
-2.1±0.4 Sv
+0.6±0.3Sv
-1.0±0.4 Sv
Summer
e)
+2.0±0.6 Sv
+1.1±0.3 Sv
+3.2±0.4 Sv
+2.5±0.7 Sv
+ 1.3±0.2 Sv
+2.4±0.5 Sv
-1.4±0.6 Sv
+1.7±0.4 Sv
+ 1.1±0.3 Sv
Fall
Latitude (°N)
Longitude (°W)

Figure 5

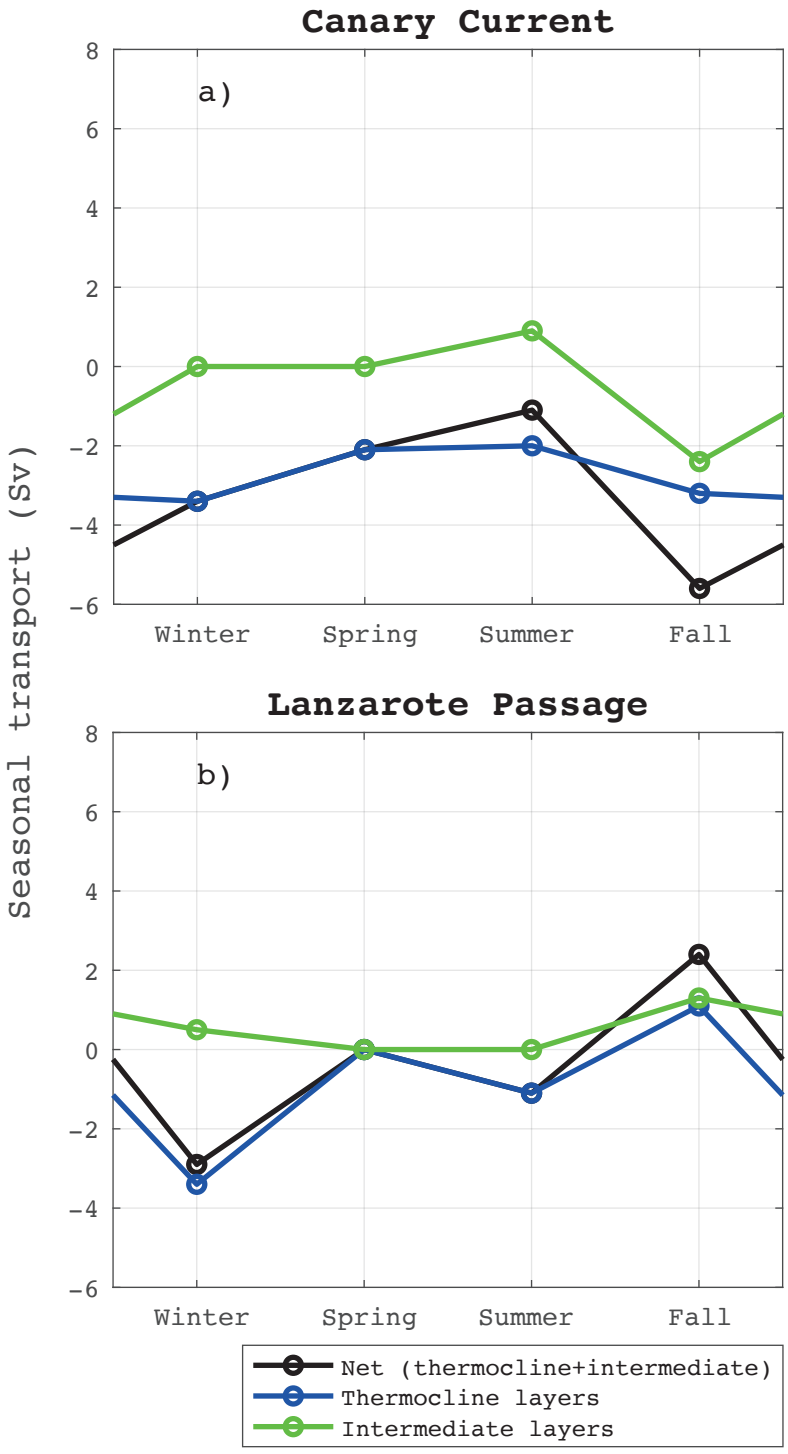
Canary Current
a)
Lanzarote Passage
b)
Seasonal transport (Sv)
8
6
4
2
0
−2
−4
−6
Winter
Spring
Summer
Fall
Net (thermocline+intermediate)
Thermocline layers
Intermediate layers

Figure 6

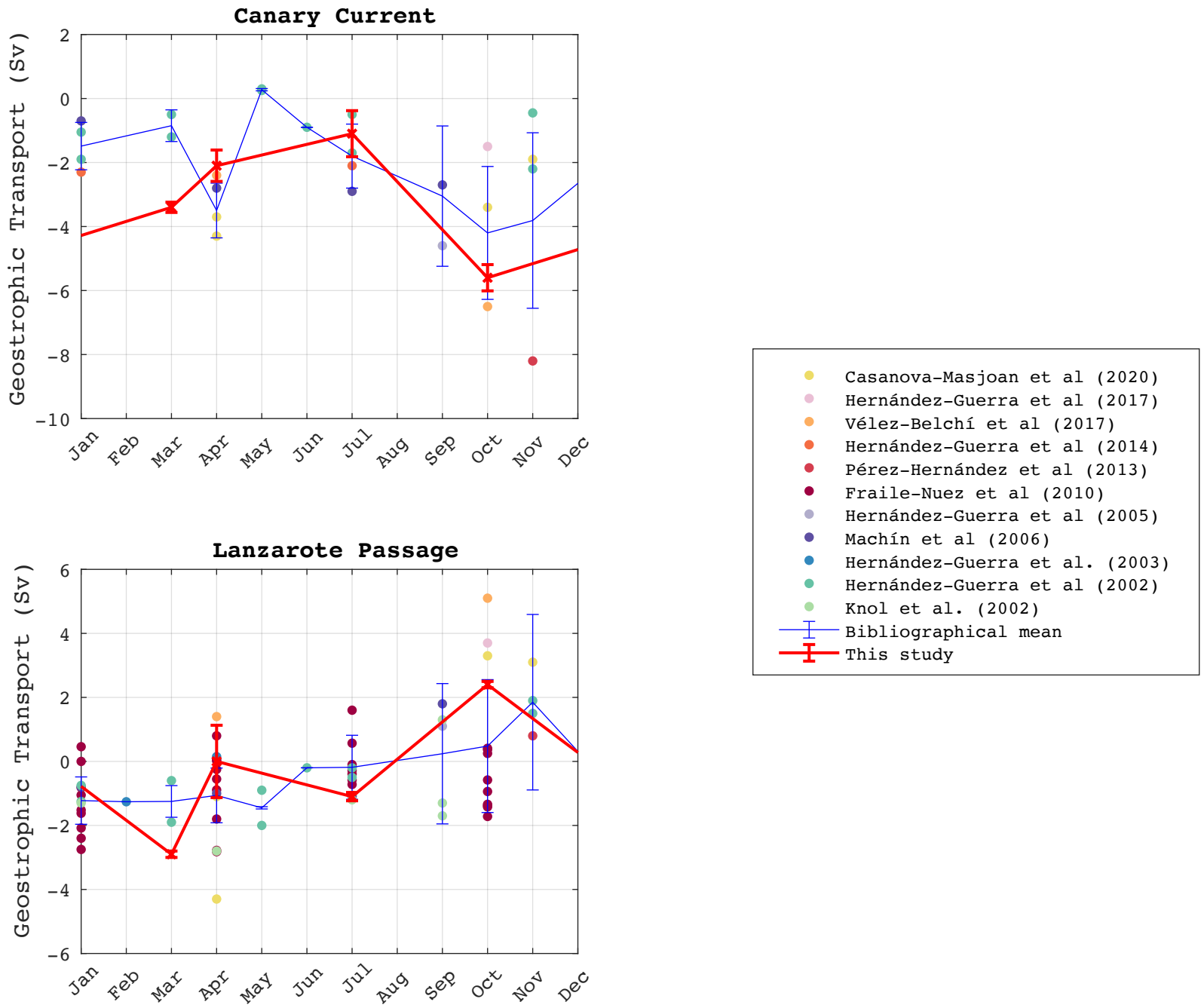
Canary Current
Geostrophic Transport (Sv)
2
0
−2
−4
−6
−8
−10
Jan
Feb
Mar
Apr
May
Jun
Jul
Aug
Sep
Oct
Nov
Dec
Lanzarote Passage
Geostrophic Transport (Sv)
6
4
2
0
−2
−4
−6
Jan
Feb
Mar
Apr
May
Jun
Jul
Aug
Sep
Oct
Nov
Dec
Casanova-Masjoan et al (2020)
Hernández-Guerra et al (2017)
Vélez-Belchí et al (2017)
Hernández-Guerra et al (2014)
Pérez-Hernández et al (2013)
Fraile-Nuez et al (2010)
Hernández-Guerra et al (2005)
Machín et al (2006)
Hernández-Guerra et al. (2003)
Hernández-Guerra et al (2002)
Knol et al. (2002)
Bibliographical mean
This study

Figure 7

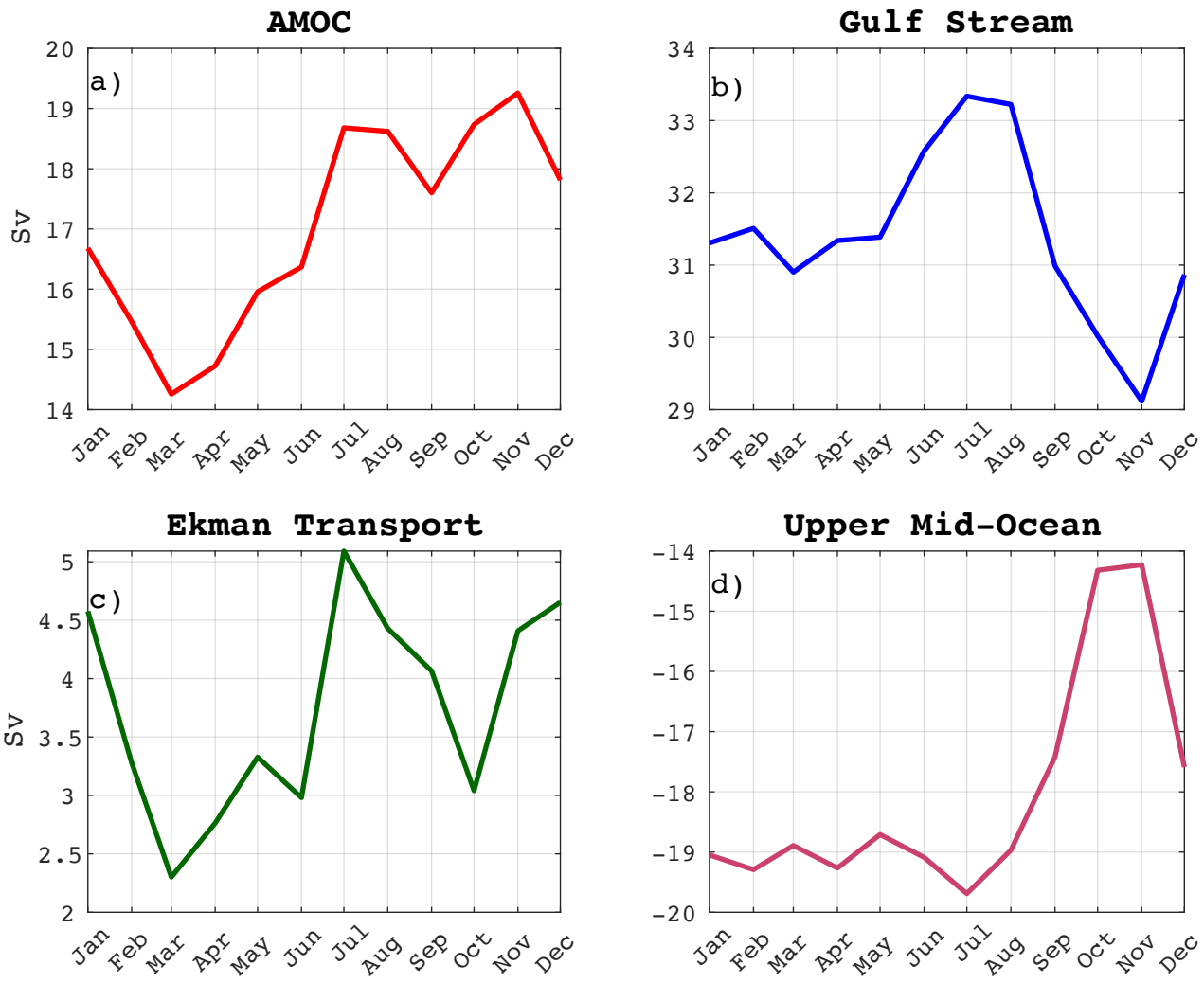
AMOC
a)
Sv
20
19
18
17
16
15
14
Jan
Feb
Mar
Apr
May
Jun
Jul
Aug
Sep
Oct
Nov
Dec
Gulf Stream
b)
34
33
32
31
30
29
Ekman Transport
c)
Sv
5
4.5
4
3.5
3
2.5
2
Upper Mid-Ocean
d)
-14
-15
-16
-17
-18
-19
-20

Figure 8

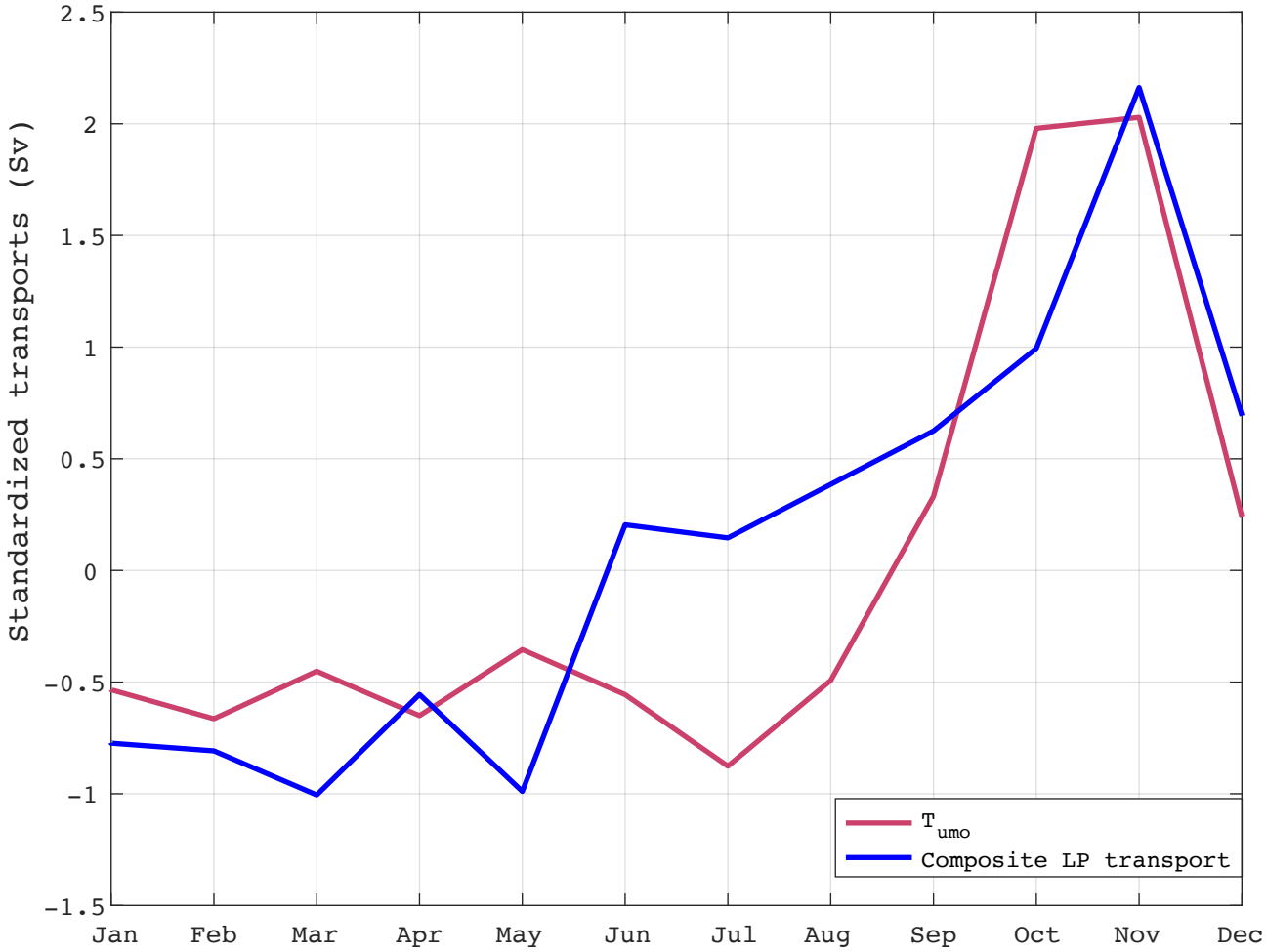
Standardized transports (Sv)
2.5
2
1.5
1
0.5
0
-0.5
-1
-1.5
Jan
Feb
Mar
Apr
May
Jun
Jul
Aug
Sep
Oct
Nov
Dec
T umo
Composite LP transport

Figure 9